Reconciling the conflict between optical transparency and fouling resistance with nanowrinkled surface inspired by zebrafish's cornea

Andre E. Vellwock[a], Pei Su[b], Zijing Zhang[a], Danqing Feng[b,], Haimin Yao[a,*]*

[a]Department of Mechanical Engineering, The Hong Kong Polytechnic University, Hung Hom, Kowloon, Hong Kong SAR 999077, China

[b]State-Province Joint Engineering Laboratory of Marine Bioproducts and Technology, College of Ocean and Earth Sciences, Xiamen University, Xiamen 361102, China

[*]Corresponding authors. E-mail: mmhyao@polyu.edu.hk (H. Yao), dqfeng@xmu.edu.cn (D. Feng)

Keywords: transparency, fouling, surface engineering, bioinspiration, zebrafish

Abstract

Surface topography has been demonstrated as an effective non-chemical strategy for controlling the fouling resistance of a surface, but its impact on optical transparency remains a barrier to the application of this strategy in optical materials. To reconcile the conflicting effects of surface topography on optical transparency and fouling resistance, here we study the optical properties and antifouling performance of nanowrinkled surfaces inspired by the corneal surface of zebrafish (*Danio rerio*). Experimental and numerical analysis demonstrates that a good compromise between optical transparency and antifouling efficacy can be achieved by wavy nanowrinkles with a characteristic wavelength of 800 nm and amplitude of 100 nm. In particular, the optimal wrinkled surface under study can reduce biofouling by up to 96% in a single-species (*Pseudoalteromonas* sp.) bacterial settlement assay in laboratory and 89% in a

field test while keeping the total transmittance above 0.98 and haze below 0.04 underwater. Moreover, our nanowrinkled surface also exhibits excellent resistance against contamination by inorganic particles. This work provides a non-chemical strategy for achieving the coexistence of optical transparency and fouling resistance on one single material, which implies significant application potential in various optical devices and systems, such as antibacterial contact lenses and self-cleaning solar panels.

Introduction

Optical surfaces applied in harsh environments are prone to the accretion of foreign matters, including organic and inorganic molecules, particles, bacteria and viruses, and even sessile animals, leading to functional and economic detriments in a broad spectrum of applications. For instance, healthcare products[1] such as endoscopic cameras and contact lenses tend to be colonized by bacteria, resulting in high infection risks to patients and users. The attachment and proliferation of sessile animals in the ocean, such as barnacles and tubeworms, on underwater cameras and submarine windows cause material deterioration and loss of vision (**Figure S1**), ruining the optical functionality of the concerned devices.[2] Desert solar farming, an emerging industry for collecting solar energy, suffers from the accumulation of sand, dust, and other inorganic particles on solar panels, which drastically reduce the efficiency of energy conversion.[3] Controlling the accretion and fouling of other matters on these optical surfaces is challenging since the potential solutions to preventing fouling tend to interfere with optical transparency.

To reconcile the conflict between fouling resistance and optical transparency, different strategies have been proposed.[4-10] For example, chemical coatings were applied to reduce fouling attachment with no significant sacrifice of the optical transparency;[6, 9] however, the compositions of these coatings might be chemically active[11] and may bring adverse side effects

to the potential users. For example, some toxic chemical compounds have been shown to cause drastic alterations to ecosystems such as physiological alterations on mollusks and fishes,[12, 13] and broad waterways contaminations.[14] Topographical modifications such as the inclusion of micro- and nano topographical features have been confirmed as an effective and environmentally friendly method to enhance fouling resistance of surfaces,[15, 16] but their influence on the optical properties is not well understood. A film with nanowires deposited on the surface achieved superior resistance to marine fouling and acceptable transmittance of light, but its high degree of haze may affect its visual quality.[7] Nanospikes inspired by moth-eye showed good optical transparency and acceptable fouling resistance which relied on surface chemical treatments.[5, 10] Liquid-infused porous surfaces (SLIPS) offered promising fouling resistance against marine algae,[4] blood, and mucus.[8, 17] Despite their high optical transparency, they require frequent refilling of lubricants.[8] Moreover, their high manufacturing costs are also a barrier to mass production.[18] By far, strategies for compromising the conflict between fouling resistance of surface topographies and the accompanying interference with the optical transparency are still in urgent need.

To explore the non-chemical solutions to reconcile the conflict between optical transparency and fouling resistance, we cast our attention to Mother Nature with a focus on the corneal tissues of fishes which are believed to encounter the similar challenge as we do and most probably have already found effective solutions through millions of years of evolution. Earlier anatomical studies revealed that the outer surface of the cornea of zebrafish (*Danio rerio*) is covered with nanowrinkles.[19] Similar nano topographies but of different geometries were also observed on the corneal tissue of other vertebrates,[20-22] such as mammals,[20] including humans,[23] fishes,[19, 21, 22, 24] and even invertebrates such as cephalopods.[25] Possible functions of these surface features include tear film stability,[20, 23] anti-reflectivity,[25] and nutrient and gas interchange.[22] Here, we propose a hypothesis that these nanowrinkles help resist fouling while

preserving the optical transparency of the tissue. To testify this hypothesis, we synthesized a series of bioinspired surfaces with wavy wrinkles ranging from 325.7 to 6741 nm in lateral wavelength and 1.2 to 685.7 nm in amplitude. An integrated experimental and numerical analysis was carried out to investigate the effects of the wrinkles' geometrical features on the film's optical transparency and fouling resistance, respectively. Our results show that low light scattering and high transmittance are achieved underwater when the amplitude of the wrinkles is reduced to below 300 nm. On the other hand, the fouling resistance is mostly affected by the wavelength of the waviness. Settlement assay indicated that the fouling extent can be reduced when the wavelength is in the range of 500-1100 nm. This range for optimal fouling resistance is similar to the characteristic wavelength of the nanowrinkles observed on the corneal surface of zebrafish. Our best bioinspired surface avoided fouling by 96% in a laboratory assay with the bacterium *Pseudoalteromonas* sp. and by 89% in a field test in ocean. Our results provide an effective, scalable, non-chemical solution to reconcile the conflict between optical transparency and fouling resistance, and it is of great value to the development of shielding films for optical instruments working in unfavorable environments.

Results and Discussions

Surface topography of the corneal tissue of zebrafish

The zebrafish (*Danio rerio*) (**Figure 1**a) does not have eyelids and, therefore, its cornea, as the outmost ocular tissue, is directly subjected to the fouling pressure from the environment (**Figure 1**b). Scanning electron microscopy (SEM) of the corneal tissue displays a surface covered with randomly distributed nanowrinkles (**Figure 1**c). Topographical scanning through atomic force microscopy (AFM) shows that the wrinkles' average amplitude, namely half of the peak-to-valley distance, is around 73.5 nm (**Figure 1**d). The Fast Fourier Transformation

(FFT) of the AFM-based topography displays peaks radially symmetrical to the center (inset of **Figure 1**d), from which the average wavelength of the wrinkles (λ_{avg}) is determined to be around 440 nm (**Figure 1**e) (see Experimental Section). Numerical simulation based on the topography obtained by AFM scanning indicates that such nanowrinkles would not affect the total transmittance and the haze of the tissue too much in the visible light spectrum (380-700 nm) in air. The optical performance underwater is even better owing to the similar refractive indexes between the corneal tissue (1.30[26]) and water (1.33[27]) (**Figure S2**).

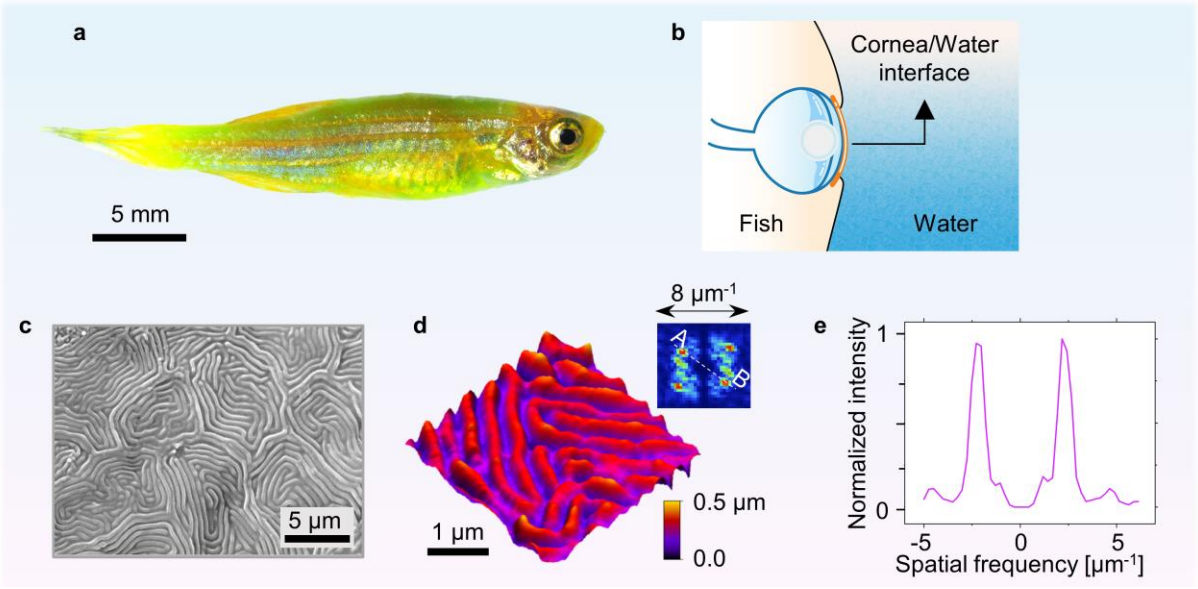

Figure 1. (a) Zebrafish (*Danio rerio*). (b) Schematics showing the interface between the fish's eye and the aquatic environment. (c) SEM image of the external surface of the corneal tissue and (d) topography imaging of the external surface using AFM and its 2D FFT pattern. (e) Line profile (A-B in the inset of d) extracted from the 2D FFT pattern.

Bioinspired nanowrinkled surfaces

Inspired by the nanowrinkles on the surface of zebrafish's cornea, we fabricated wrinkled surfaces by taking advantage of the mechanical instability of thin-film coatings. Typically,

when a stiff coating on a thick elastomeric substrate is subjected to in-plane compression strain ε, lateral buckling of the coating happens when the compression reaches a critical level, resulting in wavy wrinkles. Elastic buckling theory predicts that the amplitude and wavelength of the resulting wrinkles are given by[28]

$$A = h_{\mathrm{f}}\sqrt{4\varepsilon\left(\frac{\bar{E}_{\mathrm{f}}}{3\bar{E}_{\mathrm{s}}}\right)^{2/3} - 1}\,, \quad \lambda = \pi h_{\mathrm{f}}\left(\frac{8\bar{E}_{\mathrm{f}}}{3\bar{E}_{\mathrm{s}}}\right)^{1/3} \qquad (1)$$

where h_{f} is the thickness of the coating and $\bar{E}_{\mathrm{f}}$ and $\bar{E}_{\mathrm{s}}$ stand for the plane strain moduli of the coating and substrate, respectively. The dependence of these two characteristic length scales of the wrinkles on the mechanical properties of the coating substrate, coating thickness as well as the applied compressive strain ε allows us to fabricate wrinkles with controllable amplitudes and wavelengths. Here, we treated a pre-stretched PDMS film with oxygen plasma, which breaks the Si-CH_3 groups, yielding a glass-like stiffer Si-O_x layer.[29] (**Figure S3**a).

After releasing the pre-strain, denoted by $\varepsilon_{\mathrm{pre}}$, wavy wrinkles appear on the surface due to the buckling of the stiffer coating upon the contraction of the elastic substrate (**Figure S4**). By controlling the pre-strain and the plasma exposure time, which affects the modulus of the coating, we fabricated surface wrinkles with amplitude (A) ranging from 1.2 to 685.7 nm and wavelength (λ) spanning from 325.7 to 6741 nm (**Figure 2**a). The wavelength is mainly influenced by plasma exposure time (**Figure S5**a), while the amplitude is determined by both pre-strain and time of plasma exposure (**Figure S5**b). This is consistent with the prediction by the buckling theory as described in Eq. (1). The steepness of the nanowrinkles, which is characterized by the amplitude to wavelength ratio (A/λ), falls in the range of $4.83 \cdot 10^{-4} < A/\lambda < 0.23$ (**Figure 2**a). The contact angles (with water) of the wrinkled surfaces were measured along the directions parallel and perpendicular to the groove lines, respectively (**Figure 2**b and **S6**a), showing hydrophobicity of the wrinkled surfaces (**Figure S6**b).

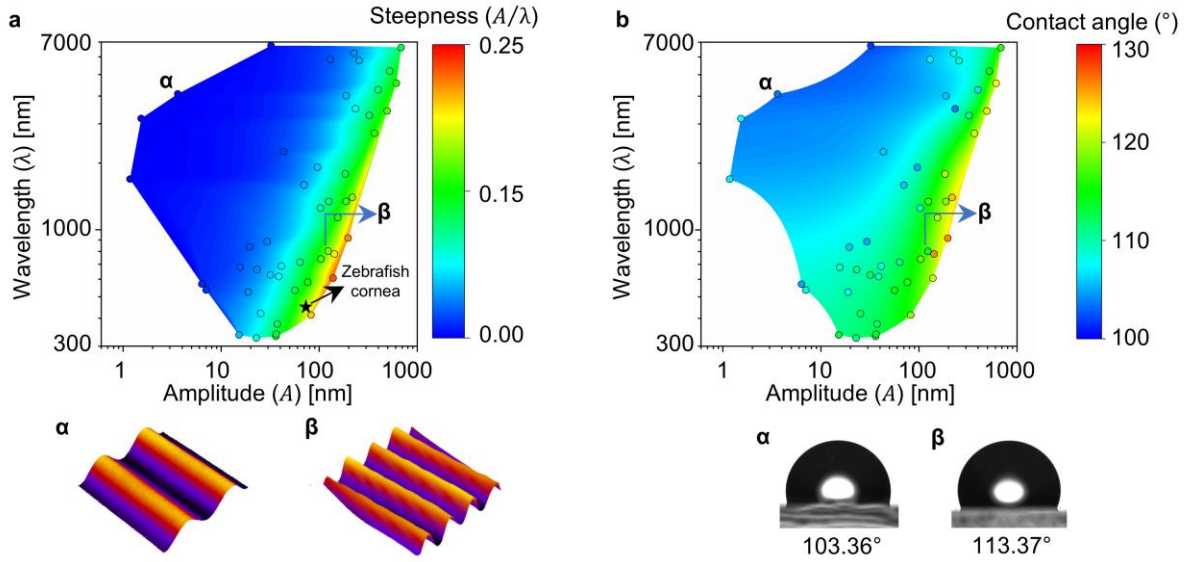

Figure 2. (a) The distributions of amplitude (A), wavelength (λ), and steepness (A/λ) of the prepared nanowrinkle. The star symbol indicates the position of the nanowrinkles on the corneal surface of zebrafish ($A = 73.5$ nm, λ_{avg}= 440 nm). Here, A is calculated from the surface arithmetical mean roughness (R_a) through $A = \frac{\pi}{2}R_a$. The topographies of two representative surfaces (denoted as α and β) measured by AFM are shown with amplitude magnified by 200 and 2 times respectively for better visualization. (b) Contact angles of the prepared nanowrinkled surfaces measured along the direction parallel to the grooves.

Optical properties of the bioinspired nanowrinkled surfaces

To reveal the dependence of the optical properties, which are characterized by the total transmittance and haze, of the fabricated surfaces on the amplitude and wavelength of the surface nanowrinkles, experimental measurements and computational simulations were carried out (see Experimental Section). Total transmittance (T_{total}) refers to the ratio of the transmitted light's intensity to the incident light's intensity irrespective of the direction of the light transmitted. Haze (H) is the fraction of the diffused light in the total transmitted light. In

practice, any transmitted light that scatters more than 2.5° from the direction predicted through Snell's law is counted as diffused light. For high optical transparency, materials should have not only high total transmittance (*e.g.*, $T_{\text{total}} > 90\%$) but also low haze (*e.g.*, $H < 5\%$). **Figure 3**a and **3**c show that the amplitude of the wrinkles, compared to their wavelength, plays a more important role in determining the haze of the surface, irrespective underwater or in air. The smaller the amplitude, the lower the haze. For a given wrinkled surface, the haze underwater is lower than that in air. This is mainly because the refractive index of PDMS (1.35-1.46, **Figure S7**a) is closer to that of seawater (1.34[30]) than to that of air (1.0[31]). For the total transmittance, most of the wrinkled surfaces exhibit a value higher than 90% (**Figure 3**b and **3**d). This is mainly due to the intrinsic high transparency of PDMS material and the small thickness (3 mm) of the samples. To examine the visual quality through these wrinkled surfaces, we put the samples in front of a digital camera and took pictures of the same object (a Snellen eye chart) underwater and in air. **Figure 3**e shows the pictures taken in the front of the selected samples. It can be seen that the visual quality becomes worse as the haze of the sample increases even though the total transmittance is kept above 90%. Moreover, for the same sample, the visual quality underwater is better than that in air. This can be attributed to the relatively lower haze of the sample underwater.

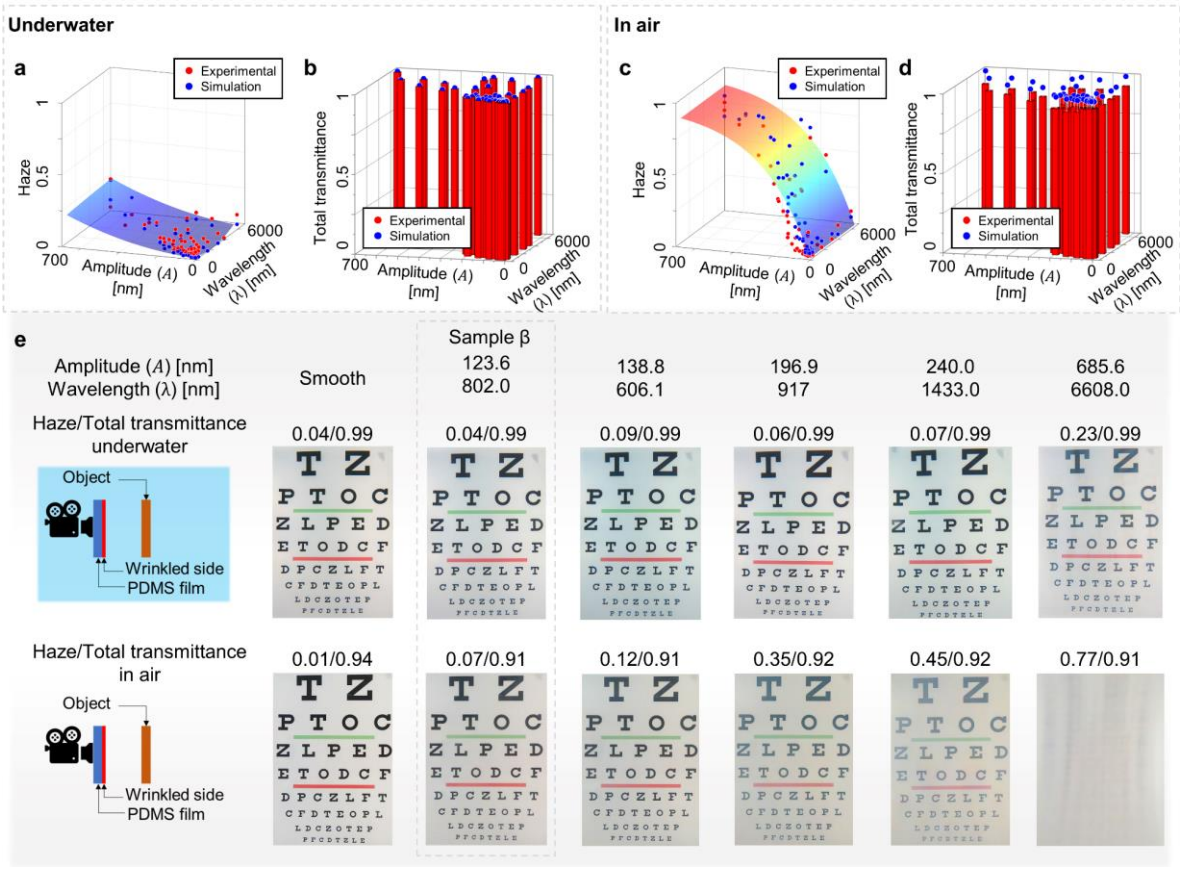

Figure 3. Optical properties of the bioinspired nanowrinkled surfaces. Measured and calculated haze and total transmittance (a, b) underwater and (c, d) in air. The continuous surfaces in (a) and (c) are the fitting surfaces of the scattered simulated data. The coefficients of determination (R^2) between the experimental data and the corresponding fitting surface in (a) and (c) are 0.91 and 0.62 respectively, highlighting the capacity of the computational model to predict the experimental results. (e) Digital pictures of a Snellen eye chart taken by a digital camera with the lens covered by different nanowrinkled surfaces underwater and in air.

Fouling resistance of the bioinspired nanowrinkled surfaces

To assess the fouling resistance of the fabricated nanowrinkled surfaces, a laboratory settlement assay was carried out with the bacterium *Pseudoalteromonas* sp., which is a species

of marine bacterium often applied in biofouling assessment.[32-34] The dependence of the normalized fouling intensity on the wrinkles' amplitude and wavelength is shown in **Figure 4**a with statistical significance described in **Table S1**. In **Figure 4**a, the fouling intensity is measured by the areal density of the attached bacteria on the tested surface normalized by that on a smooth control (SC) surface without being treated with plasma. It can be seen that surface wrinkles ranging from 600-1000 nm (*e.g.*, sample β) can reduce fouling by 80% as compared to the smooth control. However, surface topography does not always benefit fouling resistance. Our results show that when the wrinkle wavelength increases to 2 μm and the amplitude exceeds 200 nm (*e.g.*, sample η), the fouling resistance of the wrinkled surface becomes even worse than that of the smooth control. Since the fouling resistance shown in **Figure 4**a may include the contribution from the plasma treatment, which was found to reduce the contact angle and increase the elastic modulus of PDMS (**Figure S3**), we thereby calculated the topographical contribution through $TC = \frac{(C_{\mathrm{smooth-p}} - C_{\mathrm{wrinkle}})}{C_{\mathrm{smooth-p}}}$, where C_{wrinkle} is the fouling intensity (normalized) of the wrinkled surface (**Figure 4**a), and $C_{\mathrm{smooth-p}}$ the fouling intensity (normalized) of the corresponding smooth PDMS surface treated with the same plasma exposure (**Figure S8**a). Based on the calculated TC for all the wrinkled surfaces, we plot the fitted contour of TC as a function of the amplitude and wavelength of the wrinkles (see **Figure 4**b). It can be seen that wrinkles can either enhance ($TC > 0$) or reduce ($TC < 0$) the fouling resistance of the surface, depending on the wavelength and amplitude. Wrinkles with wavelength below 500 nm were found to reduce the fouling resistance of the concerned surface. Wrinkles with wavelength ranging from 500 nm to 1.1 μm were found to enhance the fouling resistance against *Pseudoalteromonas* sp. Such enhancement seems independent of the amplitude of the wrinkles, at least in the tested range of $3\ \mathrm{nm} < A < 200\ \mathrm{nm}$. In view of the characteristic dimensions of the bacterium *Pseudoalteromonas* sp. (1.27 ± 0.23 μm in width,

1.99 ± 0.34 μm in length), the existence of such optimal wavelength range with superior fouling resistance can be well explained by the least-adhesion-force theory which indicates that surface topography with inter-asperity spacing slightly smaller than the fouler's size gives rise to the least adhesion force with the fouler and therefore best fouling resistance.[35] When the inter-asperity spacing exceeds a threshold, the fouling resistance decreases as the fouler can reach the wrinkle's concave trough, where higher adhesion force can be achieved. [35] In our case, this situation occurs when the wrinkle wavelength exceeds 1.1 μm especially when the amplitude $A > 200$ nm. However, when wavelength exceeds 3 μm, the fouling resistance of the wrinkled surface is getting close to that of a smooth surface with slight fluctuation near the neutral line ($TC = 0$) which might be attributed to experimental error. Optical microscopy images of fouled samples β and η highlight the contrast of fouling resistance between them (**Figure 4**c).

To further assess the fouling resistance of the wrinkled surfaces in the environment with multiple fouling species, a field test was carried out (see Experimental Section). The fouling intensity on the wrinkled surfaces normalized by that on the smooth control surface is shown in **Figure 4**d with statistical significance given in **Table S2**. Here, the fouling intensity is measured by the fouling percentage cover on the tested surface normalized by that on a smooth control (SC) surface without being treated with plasma. Among all the tested samples, sample β ($\lambda = 802$ nm, $A = 123.6$ nm) showed the best fouling resistance in the field test with 89% reduction in fouling intensity as compared to the smooth control (p-value < 0.01, see **Table S2**), while the worst sample γ ($\lambda = 1.588$ μm, $A = 70.2$ nm) exhibited only 8% fouling reduction. Similarly, based on the results of the corresponding smooth plasma-treated surfaces (**Figure S8**b), the topographical contribution (TC) to the fouling resistance in the field test was calculated and shown in **Figure 4**e. Most of the wrinkled surfaces promoted fouling resistance in the field test, with the best performance exhibited by the sample β ($\lambda = 802$ nm, $A =$

123.6 nm). This is consistent with the results in the laboratory assay above. However, there are wrinkles with $\lambda \approx 3$ μm and $A \approx 200$ nm (*e.g.*, sample η) found to reduce the fouling resistance in the field test. The SEM images of samples β and γ are shown in **Figure 4**f. To identify the wrinkle which reconciles the conflict between optical transparency and fouling resistance to the best, we integrated the results of optical properties (haze underwater and in air) and fouling intensity in laboratory assay and field test, as shown in **Figure 5**. It can be seen that sample β exhibits the best fouling resistance in both laboratory assay and field test, while its haze is less than 0.04 underwater and 0.07 in air. The optical properties of sample β in the whole visible light spectrum are detailed in **Figure S9**.

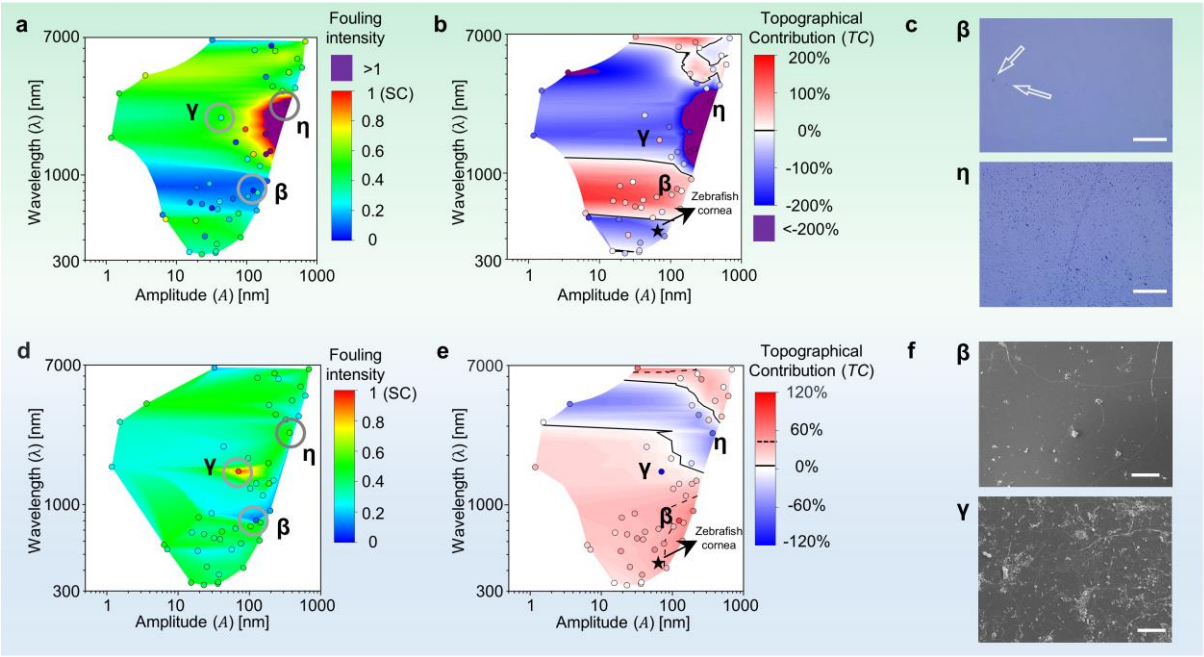

Figure 4. (a) Effects of wavelength and amplitude of the surface wrinkles on fouling intensity measured in laboratory assay. Here, fouling intensity is measured by the areal density of the attached bacteria on the tested surfaces normalized by that on the smooth control (SC). (b) The topographical contribution (TC) to fouling resistance, where the solid line delineates $TC = 0\%$. (c) Optical microscopy images illustrating the samples with the highest and lowest normalized fouling intensities. (d) Effects of wavelength and amplitude of surface wrinkles on fouling

intensity measured in marine field tests. Here, fouling intensity is measured by the fouling percentage cover normalized by the value of the SC. (e) The topographical contribution to fouling resistance, where the solid line delineates $TC = 0\%$ and the dashed line marks the $TC = 40\%$. (f) SEM images of the attachment of marine microorganisms after the field test. Bacterial assay scale bars: 50 μm. Field test scale bars: 200 μm.

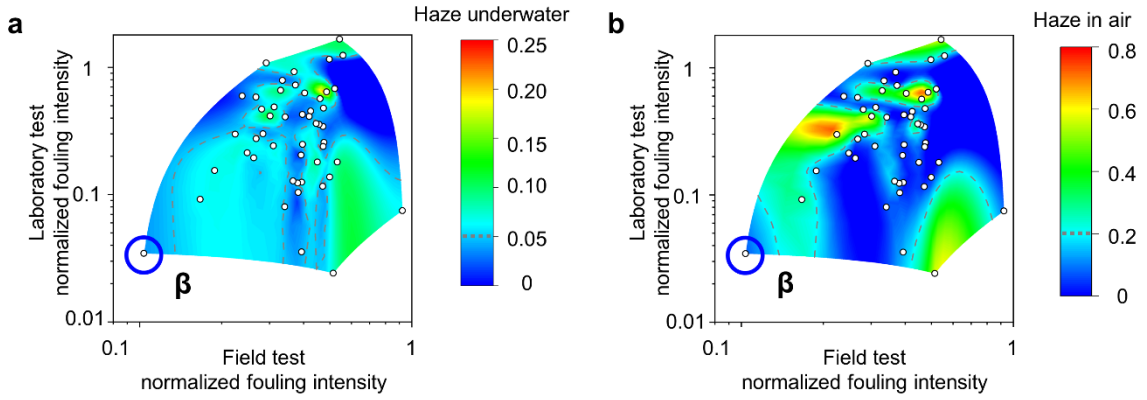

Figure 5. (a) Optimization plots show the trade-off between field and laboratory fouling and haze (a) underwater and (b) in air.

In addition to the fouling resistance against organic molecules and bacteria, our transparent nanowrinkled surfaces also exhibit superior resistance against the attachment of the inorganic particles (**Figure 6**). For example, it is much easier to remove the cement powder on sample β by dropping water or mechanical shaking (**Figure 6**b and **6**c) as compared to the smooth control (see **Figure S10** for the surface topographical data), implying the great application potential as the shield for solar panels in desert. After removing the cement particles by mechanical shaking, sample β exhibits a better transparency ($T_{\text{total}} = 87\%, H = 9\%$) in comparison to the smooth control ($T_{\text{total}} = 56\%, H = 46\%$) (**Figure S11**). If rinsed with water drops, the optical transparency of sample β can be recovered fully, while that of the smooth surface cannot be

(**Figure S11**). Moreover, in addition to planar surfaces, nanowrinkles can also be produced on curved surfaces by using a similar pre-straining technique (see Experimental Section for details), implying the great application promise of our transparent fouling-resistant surfaces in contact lenses (**Figure 6**d).[36, 37] For this application, the optimal wrinkle (sample β) we found above may not apply since the micro protrusions on human cornea, if they are also for resisting biofouling, exhibit similar amplitude (mean height ~129 nm[38]) but much shorter wavelength ($\lambda = 47$ nm).[23] As the optimal wrinkle dimensions depend on the sizes of the potential bacteria, a further investigation is needed to determine the best surface wrinkles for contact lenses.

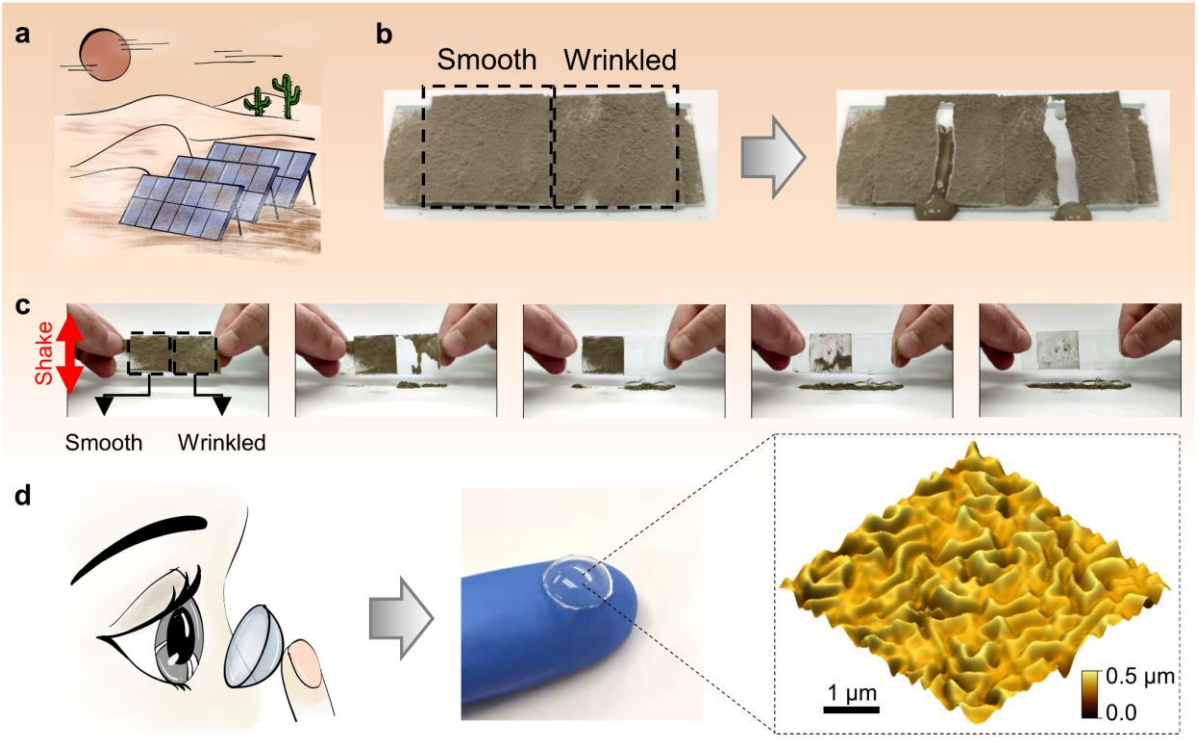

Figure 6. (a) Schematic illustration showing the dust-covered solar panels in a desertic environment. (b) Demonstration of the self-cleaning property of the bioinspired nanowrinkled surfaces upon (b) water dropping and (c) mechanical shaking. (d) A curved membrane with nanowrinkled surface implies great application promise in contact lenses. The amplitude in the AFM topography is exaggerated by 30 times for better visualization.

Conclusions

Inspired by the surface topography on the cornea of zebrafish, we synthesized polymeric films with controllable surface nanowrinkles by taking advantage of the buckling phenomenon of stiffer coating on a soft foundation under compression. By investigating the effect of the wrinkles' size on the haze and total transmittance of the film, which are two indexes characterizing optical transparency, we found that the wrinkle amplitude plays the dominant role in determining the optical transparency of the film. In particular, our results showed that wrinkles with amplitude ~300 nm or less can achieve satisfactory optical transparency (haze < 10% and total transmittance >90%). On the other hand, the fouling resistance of the films depends more on the wrinkle wavelength than on the amplitude. Our results showed that wrinkles with a wavelength around 800 nm exhibit the best fouling resistance in both laboratory assay with a bacterium and field tests in the ocean with multiple fouling species. In addition, the optimal wrinkled surface with $\lambda \approx 800\ \mathrm{nm}$, $A \approx 100\ \mathrm{nm}$ was found resistant to the attachment of inorganic particles as well. Our results provide a non-chemical solution to reconciling the conflict between optical transparency and fouling resistance and are of great value to the design of shields for optical instruments working in extreme environments such as solar panels in the desert and deep-sea cameras.

Experimental Section

Characterization of corneal tissue of zebrafish

Adult zebrafish (*Danio rerio*) were purchased from a local aquarium fish market. Ocular tissue was extracted from the zebrafish following the guidelines (ARVO Statement for the Use of Animals in Ophthalmic and Vision Research) The fisheyes were fixed overnight in cacodylate buffer (0.1 M) with 2.5% glutaraldehyde and 2% formaldehyde at 4 °C, washed with

cacodylate buffer before a 2 h postfixation with 2% osmium tetroxide in the same buffer. Samples were rinsed with deionized water and dehydrated in graded ethanol series (30%, 50%, 70%, 90%, 100%, 100%; 10 min each step). The cornea exterior surface was observed with a scanning electron microscope (Vega 3, Tescan). Topographical data was acquired with atomic force microscopy (Nanoscope 8, Bruker) and analyzed with imaging software (Gwyddion[39]). The average wavelength of the wrinkles was assessed by the inverse average of peak-to-center radial distance in the 2D FFT pattern.

Fabrication of bioinspired nanowrinkled surfaces

Polydimethylsiloxane (PDMS, Sylgard 184, Dow Corning) base and curing agent were mixed in a mass ratio of 10:1. The uncured PDMS was poured into a glass mold (70 mm × 30 mm × 3 mm), after degassing, curing overnight at 60 °C, and demolding, a flat PDMS strip was obtained. Then, the PDMS strip was mounted on a homemade stretcher (**Figure S4**a), which can controllably apply tensile pre-strain on the strip (**Figure S4**b). The pre-strained PDMS strip was then treated with oxygen plasma (45W, PDC-002 Plasma Cleaner, Harrick) for some time (**Figure S4**c). After releasing the strain on the strip, surface wrinkles were produced on the strip's top surface (**Figure S4**d). The characteristic dimensions (amplitude and wavelength) of the wrinkles were tuned by controlling the pre-strain (up to 70%) and the plasma exposure time in the range of 30-2000 s (**Figure S4**e).

To produce wrinkles on a curved surface, uncured PDMS was poured onto a glass semisphere (diameter: 14 mm) attached on a flat glass slide and quickly placed in an oven (120 °C) for 10 min for curing. This step was repeated two times. After demolding, a PDMS film with a semispherical shell was obtained. Then, this film was pre-strained by pressing a larger glass semisphere (diameter: 16 mm) into the concave pocket and treated with oxygen plasma (45 W, PDC-002 Plasma Cleaner, Harrick) for 250 s. After releasing the strain by removing the glass

semisphere, nanowrinkles were produced on the semispherical PDMS shell as confirmed by atomic force microscopy.

Topographical and modulus characterizations

Atomic force microscopy (Nanoscope 8, Bruker) in tapping mode was applied to characterize the surface topography of the wrinkled surfaces. To measure the effect of plasma treatment on the modulus of PDMS, nanoindentation tests were carried out on smooth PDMS films treated with plasma using atomic force microscopy (Nanoscope 8, Bruker) in force-volume contact mode.

Wettability measurement

The contact angles of surfaces were measured using an optical tensiometer (Theta, Biolin Scientific) with a deionized water drop of 3 μL. During the experiments, the room temperature was kept constantly at 22°C. Five measurements were performed for each sample. Measurements were made after at least two weeks after the plasma treatment so that the temporary hydrophilicity of PDMS caused by plasma treatment disappeared.[40]

Characterization of optical properties

Optical properties, such as total and diffusive transmittance, of the samples were measured with a spectrophotometer (Lambda 1050 with integrating sphere, PerkinElmer). Film samples were positioned with their surfaces perpendicularly to the light source. To measure the underwater properties, samples were placed in a cuvette filled with artificial seawater (DI water, 3.5 wt.% artificial aquarium sea salt). The light source was set to the visible light (wavelength:

380-700 nm). Haze was calculated as a ratio between the diffusive transmittance and the total transmittance.

Computation of optical properties

The optical properties of a film with wrinkled surfaces were also computed with software FDTD Lumerical based on a model schematically shown in **Figure S7**b. A normally incident plane wave (wavelength: 380-700 nm) was set to shoot directly at the surface. Below the wrinkled surface, the light waves transmitted through the material, and their angles are measured on the assessing plane. If the angle is not perpendicular to the surface by more than 2.5°, the transmittance is deemed as diffusive. Otherwise, the transmittance is specular. For the synthetic surface, due to the topography periodicity, only one period is considered. For the zebrafish's corneal tissue, a larger area (2 μm × 2 μm) is considered as the wrinkles are not well aligned nor distributed. Bloch boundary conditions were applied on the lateral boundaries (BC1, BC3), while Perfectly Matched Layer (PML) boundary conditions were applied on the top and bottom boundaries (BC2, BC4). The intrinsic optical properties of the material were set based on the values experimentally measured from a smooth PDMS surface (**Figure S7**a). The surface topography of the simulated model was acquired from AFM scanning of each sample.

Characterizations of fouling resistance

The bacterial attachment assay was performed by following the protocol reported in previous studies.[32, 41] The bacterium used was the *Pseudoalteromonas* sp. W-7, which is a marine bacterium able to form strong biofilm.[42] The bacteria were isolated from a natural marine biofilm in Xiamen Bay, China, and cultured overnight in 200 mL of marine broth 2216E liquid medium on a rotary shaker (150 rpm, 28°C). Then, after being centrifuged for 5 minutes (5000

rpm, 4°C), the broth supernatant was removed, and the bacterial cells were suspended in sterile-filtered seawater (0.22 μm, FSW) to reach a density of 10^7 cells/mL. The standard 6-well plates were used in this assay, with each surface sample (5 mm × 5 mm) placed into each well together with a volume of 2 mL of bacterial suspension. A total of three replicates for each surface was evaluated. The plates were incubated for 3 h at 28 °C. Then bacterial fixation was made with 200 μL of 4% formaldehyde. After 10 min, the samples and the coverslips were washed gently with sterile FSW to remove the unattached bacteria. The attached bacterial cells on samples were stained with 0.1% crystal violet for 10 min. After being washed with distilled water, they were observed under an inverted microscope (DM IL, Leica). The number of attached bacteria was counted in ten random fields of view on each sample and averaged.

The field test was conducted at the Hebe Haven Yacht Club, Sai Kung, Hong Kong (22°21'53.0"N, 114°15'34.4"E). Samples were vertically fixated to a polymeric sheet and submerged by circa 1.5 m of seawater. After one week of submersion, samples were brought quickly to the lab, washed with cacodylate buffer (0.1 M) to remove unattached organisms, fixated overnight at 4 °C with cacodylate buffer with 2.5% glutaraldehyde and 2% formaldehyde, and dehydrated similarly to the fisheye tissue. Fouling percentage cover was assessed through scanning electron microscopy (Vega 3, Tescan). For each sample, three images were acquired at the same magnification. The figures were converted into binary mode, in which the fouled region is white, and the background is black. If necessary, minor adjustments were made (i.e., cracks in the surface were excluded). Quantification of fouling cover was made through imaging software (ImageJ). Based on the results of the laboratory assay and field test, *t*-tests were performed to evaluate the statistical significance of the fouling resistance of the wrinkled samples compared with the smooth control.

To demonstrate the resistance against the attachment of inorganic matter, cement powder (particle diameter: 6.03 ± 1.00 μm) was sieved onto the surface of the samples. Then, the

sample was tilted by 45° and splashed with DI water drops. Alternatively, the sample was continuously shaken by hand to tap the table.

Acknowledgments

The work was supported by the General Research Fund from Hong Kong RGC (PolyU 152193/14E) and the Departmental General Research Funds (G-UAHN). We would like to thank the Hebe Haven Yacht Club for their support during the field tests. A.E.V thanks S. Gao for the assistance in figure preparation.

Supporting Information Available:

Example of fouling in an underwater camera, zebrafish cornea's computed optical properties, influence of plasma on PDMS film properties, wrinkled film manufacturing schematic and the effect of pre-strain and plasma exposure to the wrinkles' dimensions and contact angle, computational model and the applied intrinsic PDMS properties, fouling intensity of smooth films with different plasma exposure, sample β optical properties in the visible light spectrum, smooth control sample's topography, optical properties of sample β and smooth sample after cleaning contamination by cement powder, the statistical significance of the results of the fouling test.

References

1. Flemming, H.-C., Microbial Biofouling: Unsolved Problems, Insufficient Approaches, and Possible Solutions. In *Biofilm Highlights*, Flemming, H.-C.; Wingender, J.; Szewzyk, U., Eds. Springer Berlin Heidelberg: Berlin, Heidelberg, 2011; Vol. 5, pp 81-109.
2. Schultz, M. P.; Bendick, J. A.; Holm, E. R.; Hertel, W. M., Economic Impact of Biofouling on a Naval Surface Ship. *Biofouling* **2011**, *27* (1), 87-98.
3. Mondal, A. K.; Bansal, K., A Brief History and Future Aspects in Automatic Cleaning Systems for Solar Photovoltaic Panels. *Adv. Robot.* **2015**, *29* (8), 515-524.

4. Chen, T.-L.; Lin, Y.-P.; Chien, C.-H.; Chen, Y.-C.; Yang, Y.-J.; Wang, W.-L.; Chien, L.-F.; Hsueh, H.-Y., Fabrication of Frog-Skin-Inspired Slippery Antibiofouling Coatings through Degradable Block Copolymer Wrinkling. *Adv. Funct. Mater.* **2021**, *31* (42), 2104173.
5. Feng, C.; Gou, T.; Li, J.; Cai, Y.; He, P.; Huang, J.; Wen, Y.; Ma, Y.; Zhang, Z., A Highly Transparent Polymer Coating on the Glass with Broadband Antireflection, Antifogging and Antifouling Properties. *Mater. Res. Express* **2019**, *6* (7), 075319.
6. Chen, R.; Zhang, Y.; Xie, Q.; Chen, Z.; Ma, C.; Zhang, G., Transparent Polymer-Ceramic Hybrid Antifouling Coating with Superior Mechanical Properties. *Adv. Funct. Mater.* **2021**, *31* (19), 2011145.
7. Wang, J.; Lee, S.; Bielinski, A. R.; Meyer, K. A.; Dhyani, A.; Ortiz-Ortiz, A. M.; Tuteja, A.; Dasgupta, N. P., Rational Design of Transparent Nanowire Architectures with Tunable Geometries for Preventing Marine Fouling. *Adv. Mater. Interfaces* **2020**, *7* (17), 2000672.
8. Sunny, S.; Cheng, G.; Daniel, D.; Lo, P.; Ochoa, S.; Howell, C.; Vogel, N.; Majid, A.; Aizenberg, J., Transparent Antifouling Material for Improved Operative Field Visibility in Endoscopy. *Proc. Natl. Acad. Sci. U.S.A.* **2016**, *113* (42), 11676.
9. Wang, W.; Lu, Y.; Zhu, H.; Cao, Z., Superdurable Coating Fabricated from a Double-Sided Tape with Long Term "Zero" Bacterial Adhesion. *Adv. Mater.* **2017**, *29* (34), 1606506.
10. Feng, C.; Zhang, Z.; Li, J.; Qu, Y.; Xing, D.; Gao, X.; Zhang, Z.; Wen, Y.; Ma, Y.; Ye, J.; Sun, R., A Bioinspired, Highly Transparent Surface with Dry-Style Antifogging, Antifrosting, Antifouling, and Moisture Self-Cleaning Properties. *Macromol. Rapid Commun.* **2019**, *40* (6), 1800708.
11. Liu, M.; Li, S.; Wang, H.; Jiang, R.; Zhou, X., Research Progress of Environmentally Friendly Marine Antifouling Coatings. *Polym. Chem.* **2021**, *12* (26), 3702-3720.
12. Blaber, S. J. M., The Ocurrance of a Penis-Like Outgrowth Behind the Right Tentacle in Spent Females of Nucella Lapillus. *J. Molluscan Stud.* **1970**, *39* (2-3), 231-233.
13. Zhao, C.-S.; Fang, D.-A.; Xu, D.-P., Toll-Like Receptors (Tlrs) Respond to Tributyltin Chloride (Tbt-Cl) Exposure in the River Pufferfish (Takifugu Obscurus): Evidences for Its Toxic Injury Function. *Fish Shellfish Immunol.* **2020**, *99*, 526-534.
14. Wang, X.; Kong, L.; Cheng, J.; Zhao, D.; Chen, H.; Sun, R.; Yang, W.; Han, J., Distribution of Butyltins at Dredged Material Dumping Sites around the Coast of China and the Potential Ecological Risk. *Mar. Pollut. Bull.* **2019**, *138*, 491-500.
15. Vellwock, A. E.; Fu, J.; Meng, Y.; Thiyagarajan, V.; Yao, H., A Data-Driven Approach to Predicting the Attachment Density of Biofouling Organisms. *Biofouling* **2019**, 1-8.
16. Vellwock, A. E.; Yao, H., Biomimetic and Bioinspired Surface Topographies as a Green Strategy for Combating Biofouling: A Review. *Bioinspir. Biomim.* **2021**, *16* (4), 041003.
17. Lee, Y.; Chung, Y.-W.; Park, J.; Park, K.; Seo, Y.; Hong, S.-N.; Lee, S. H.; Jeon, H.; Seo, J., Lubricant-Infused Directly Engraved Nano-Microstructures for Mechanically Durable Endoscope Lens with Anti-Biofouling and Anti-Fogging Properties. *Sci. Rep.* **2020**, *10* (1), 17454.
18. Heydarian, S.; Jafari, R.; Momen, G., Recent Progress in the Anti-Icing Performance of Slippery Liquid-Infused Surfaces. *Prog. Org. Coat.* **2021**, *151*, 106096.
19. Zhao, X. C.; Yee, R. W.; Norcom, E.; Burgess, H.; Avanesov, A. S.; Barrish, J. P.; Malicki, J., The Zebrafish Cornea: Structure and Development. *Investig. Ophthalmol. Vis. Sci.* **2006**, *47* (10), 4341-4348.
20. Collin, S. P.; Collin, H. B., A Comparative Sem Study of the Vertebrate Corneal Epithelium. *Cornea* **2000**, *19* (2), 218-230.

21. Collin, S. P.; Collin, H. B., The Corneal Epithelial Surface in the Eyes of Vertebrates: Environmental and Evolutionary Influences on Structure and Function. *J. Morphol.* **2006**, *267* (3), 273-291.
22. Collin, S. P.; Marshall, N. J.; Collin, H. B.; Collin, S. P., The Corneal Surface of Aquatic Vertebrates: Microstructures with Optical and Nutritional Function? *Philos. Trans. R. Soc. Lond., B, Biol. Sci.* **2000**, *355* (1401), 1171-1176.
23. Pfister, R. R.; Burstein, N. L., The Normal and Abnormal Human Corneal Epithelial Surface: A Scanning Electron Microscope Study. *Investig. Ophthalmol. Vis. Sci.* **1977**, *16* (7), 614-622.
24. Lam, P.-y.; Mangos, S.; Green, J. M.; Reiser, J.; Huttenlocher, A., In Vivo Imaging and Characterization of Actin Microridges. *PLoS One* **2015**, *10* (1), e0115639.
25. Talbot, C.; Jordan, T. M.; Roberts, N. W.; Collin, S. P.; Marshall, N. J.; Temple, S. E., Corneal Microprojections in Coleoid Cephalopods. *J. Comp. Physiol. A* **2012**, *198* (12), 849-856.
26. Collery, R. F.; Veth, K. N.; Dubis, A. M.; Carroll, J.; Link, B. A., Rapid, Accurate, and Non-Invasive Measurement of Zebrafish Axial Length and Other Eye Dimensions Using Sd-Oct Allows Longitudinal Analysis of Myopia and Emmetropization. *PLoS One* **2014**, *9* (10), e110699.
27. Hale, G. M.; Querry, M. R., Optical Constants of Water in the 200-Nm to 200-Mm Wavelength Region. *Appl. Opt.* **1973**, *12* (3), 555-563.
28. Freund, L. B.; Suresh, S., *Thin Film Materials: Stress, Defect Formation and Surface Evolution*. Cambridge University Press: Cambridge, 2004.
29. Nania, M.; Matar, O. K.; Cabral, J. T., Frontal Vitrification of Pdms Using Air Plasma and Consequences for Surface Wrinkling. *Soft Matter* **2015**, *11* (15), 3067-3075.
30. Millard, R. C.; Seaver, G., An Index of Refraction Algorithm for Seawater over Temperature, Pressure, Salinity, Density, and Wavelength. *Deep Sea Res. Part I Oceanogr. Res. Pap.* **1990**, *37* (12), 1909-1926.
31. Börzsönyi, A.; Heiner, Z.; Kalashnikov, M. P.; Kovács, A. P.; Osvay, K., Dispersion Measurement of Inert Gases and Gas Mixtures at 800 Nm. *Appl. Opt.* **2008**, *47* (27), 4856-4863.
32. Shuai, C.-X.; He, Y.; Su, P.; Huang, Q.; Pan, D.; Xu, Q.; Feng, D.; Jiang, Y., Integration of Pegylated Polyaniline Nanocoatings with Multiple Plastic Substrates Generates Comparable Antifouling Performance. *Langmuir* **2020**, *36* (31), 9114-9123.
33. Faria, S. I.; Gomes, L. C.; Teixeira-Santos, R.; Morais, J.; Vasconcelos, V.; Mergulhão, F. J. M., Developing New Marine Antifouling Surfaces: Learning from Single-Strain Laboratory Tests. *Coatings* **2021**, *11* (1), 90.
34. Lim; Everuss, K.; Goodman, A.; Benkendorff, K., Comparison of Surface Microfouling and Bacterial Attachment on the Egg Capsules of Two Molluscan Species Representing Cephalopoda and Neogastropoda. *Aquat. Microb. Ecol.* **2007**, *47*, 275-287.
35. Fu, J.; Zhang, H.; Guo, Z.; Feng, D.; Thiyagarajan, V.; Yao, H., Combat Biofouling with Microscopic Ridge-Like Surface Morphology: A Bioinspired Study. *J. R. Soc. Interface* **2018**, *15* (140), 20170823.
36. Slusher, M. M.; Myrvik, Q. N.; Lewis, J. C.; Gristina, A. G., Extended-Wear Lenses, Biofilm, and Bacterial Adhesion. *Arch. Ophthalmol.* **1987**, *105* (1), 110-115.
37. Stapleton, F.; Carnt, N., Contact Lens-Related Microbial Keratitis: How Have Epidemiology and Genetics Helped Us with Pathogenesis and Prophylaxis. *Eye* **2012**, *26* (2), 185-193.
38. King-Smith, P. E.; Kimball, S. H.; Nichols, J. J., Tear Film Interferometry and Corneal Surface Roughness. *Investig. Ophthalmol. Vis. Sci.* **2014**, *55* (4), 2614-2618.

39. Nečas, D.; Klapetek, P., Gwyddion: An Open-Source Software for Spm Data Analysis. *Open Phys.* **2012**, *10* (1), 181-188.
40. Bacharouche, J.; Haidara, H.; Kunemann, P.; Vallat, M.-F.; Roucoules, V., Singularities in Hydrophobic Recovery of Plasma Treated Polydimethylsiloxane Surfaces under Non-Contaminant Atmosphere. *Sens. Actuator A Phys.* **2013**, *197*, 25-29.
41. Kelly, S.; Jensen, P.; Henkel, T.; Fenical, W.; Pawlik, J., Effects of Caribbean Sponge Extracts on Bacterial Attachment. *Aquat. Microb. Ecol.* **2003**, *31*, 175-182.
42. Wu, Z.; Wu, Y.; Huang, Y.; He, J.; Su, P.; Feng, D., Insights into the Planktonic to Sessile Transition in a Marine Biofilm-Forming Pseudoalteromonas Isolate Using Comparative Proteomic Analysis. *Aquat. Microb. Ecol.* **2021**, *86*, 69-84.

Table of contents